

RESEARCH LETTER

10.1002/2016GL067899

Key Points:

- High-resolution topography provides a new means of mapping 3-D fault geometry
- The proposed method is complementary to the field measurements of fault dip
- From the fault geometry, we find variations in dip at the endpoint of the Hoshab rupture

Supporting Information:

- Supporting Information S1

Correspondence to:

Y. Zhou,
yu.zhou@earth.ox.ac.uk

Citation:

Zhou, Y., R. T. Walker, J. R. Elliott, and B. Parsons (2016), Mapping 3D fault geometry in earthquakes using high-resolution topography: Examples from the 2010 El Mayor-Cucapah (Mexico) and 2013 Balochistan (Pakistan) earthquakes, *Geophys. Res. Lett.*, 43, 3134–3142, doi:10.1002/2016GL067899.

Received 21 JAN 2016

Accepted 7 MAR 2016

Accepted article online 11 MAR 2016

Published online 4 APR 2016

Mapping 3D fault geometry in earthquakes using high-resolution topography: Examples from the 2010 El Mayor-Cucapah (Mexico) and 2013 Balochistan (Pakistan) earthquakes

Yu Zhou¹, Richard T. Walker¹, John R. Elliott¹, and Barry Parsons¹
¹COMET, Department of Earth Sciences, University of Oxford, South Parks Road, Oxford, United Kingdom

Abstract Fault dips are usually measured from outcrops in the field or inferred through geodetic or seismological modeling. Here we apply the classic structural geology approach of calculating dip from a fault's 3-D surface trace using recent, high-resolution topography. A test study applied to the 2010 El Mayor-Cucapah earthquake shows very good agreement between our results and those previously determined from field measurements. To obtain a reliable estimate, a fault segment ≥ 120 m long with a topographic variation ≥ 15 m is suggested. We then applied this method to the 2013 Balochistan earthquake, getting dips similar to previous estimates. Our dip estimates show a switch from north to south dipping at the southern end of the main trace, which appears to be a response to local extension within a stepover. We suggest that this previously unidentified geometrical complexity may act as the endpoint of earthquake ruptures for the southern end of the Hoshab fault.

1. Introduction

Fault traces are commonly discontinuous and separated by stepovers in map view [Wesnousky, 2006]. This geometrical complexity can play a controlling role in the nucleation and propagation of earthquakes [Kase and Day, 2006; Avouac et al., 2014]. Studies from many historical surface ruptures [Wesnousky, 2006; Elliott et al., 2015] and dynamic modeling [e.g., Harris and Day, 1999; Kase and Day, 2006; Lozos et al., 2012] have suggested that large stepovers (≥ 3 –4 km wide) are likely to arrest seismic ruptures. Furthermore, many small-scale complexities such as variations in strike and dip of fault segments within a stepover may also have an influence on rupture processes [Lozos et al., 2012]. Recent modeling studies on the 1997 Zirkuh [Sudhaus and Jónsson, 2011], 2010 El Mayor-Cucapah [Wei et al., 2011], and 2010 Darfield [Elliott et al., 2012] earthquakes using interferometric synthetic aperture radar and teleseismic waves show that fault dip may vary significantly along strike, even if the rupture appears to be continuous on the surface. Therefore, we need to fully constrain fault geometry in three dimensions (3-D) in order to better understand its role in controlling seismic ruptures.

In this study, we apply the classic structural geology approach of calculating fault dip from the surface trace as it crosses undulating topography [Tearpock and Bischke, 2002] to recent, high-resolution topography derived from light detection and ranging (lidar) and very high-resolution (VHR) (70 cm nadir resolution) Pleiades stereo imagery. Our approach is first tested on the 2010 M_w 7.2 El Mayor-Cucapah earthquake where the fault geometry has been well constrained by field observations [Fletcher et al., 2014; Teran et al., 2015] and modeling [Wei et al., 2011]. We then focus on the 2013 M_w 7.7 Balochistan, Pakistan earthquake, where it has been argued from rupture mapping using image-matching correlations that there is no clear geometrical control on the 200+ km surface rupture [Avouac et al., 2014] but where no field access is possible for testing. By reexamining the fault geometry based on Pleiades stereo imagery for the Balochistan earthquake, we find variations in dip at the end of the main trace that appear to be in response to local extension within a previously unidentified stepover and which demonstrate a possible geometrical control on rupture termination. Here we show that high-resolution topography, derived from VHR stereo imagery in particular, provides a new means of investigating the details of 3-D fault geometry at unprecedented resolution, with applicability for mapping fault ruptures and constraining structure, in places where field or airborne lidar measurements are difficult.

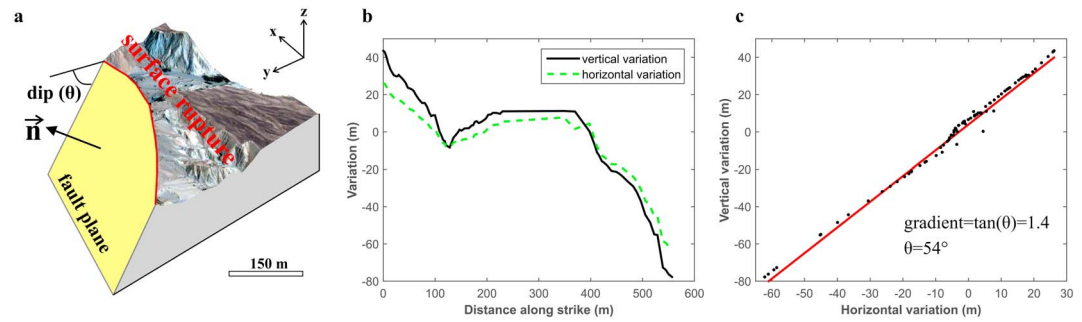


Figure 1. Measuring fault dip by fitting a plane (in yellow) to the surface rupture. (a) Cartoon showing a fault plane dipping at an angle θ to the horizontal. The normal vector of the fault plane is $\vec{n} = \left(\frac{A}{\sqrt{A^2+B^2+C^2}}, \frac{B}{\sqrt{A^2+B^2+C^2}}, \frac{C}{\sqrt{A^2+B^2+C^2}} \right)$, where A , B , C , and D are the constants in equation (1). (b) Vertical (black line) and horizontal (green dashed line) variation about the mean strike along the surface rupture. (c) Vertical variation is a linear function of horizontal variation about the mean strike (black dots are measurements from the 3-D point cloud). The gradient of the linear function (red line) is $\tan \theta$. This example is from the Balochistan earthquake (S24 in Table S1).

2. Methods

An earthquake rupture is the result of rapid slip on a fault. Assuming that the fault is planar and the rupture reaches the surface, the fault plane will intersect with the undulating topography (Figures 1a). The intersection is presented as the surface trace of an earthquake rupture. Knowing the 3-D coordinates of the intersection, we can estimate fault dip (θ in Figure 1a) by using the plane equation:

$$A \cdot x + B \cdot y + C \cdot z + D = 0 \quad (1)$$

where (x, y, z) are the coordinates of the points along the surface rupture and A , B , C , and D are unknown constants to be determined.

The orthogonal distance d_i of a point (x_i, y_i, z_i) to the plane is given by

$$d_i = \frac{|A \cdot x_i + B \cdot y_i + C \cdot z_i + D|}{\sqrt{A^2 + B^2 + C^2}} \quad (2)$$

We minimize the sum of the orthogonal distance of each point measured at the surface to the plane using a least squares regression to solve the plane equation, i.e., to estimate the parameters A , B , C , and D . The dip of the fault (θ) can then be estimated via equation (3)

$$\theta = \frac{\pi}{2} - \tan^{-1} \frac{C}{\sqrt{A^2 + B^2}} \quad (3)$$

As the surface rupture trace lies on the fault plane, for each point along the trace, the vertical variation is a linear function of the horizontal variation about the mean strike (i.e., $\tan^{-1} \frac{A}{B}$), the gradient of which is $\tan \theta$ (Figures 1b and 1c). This classic method has been successfully applied in structural geology, using three points to determine the horizontal and vertical variations and estimate the fault dip. Recent advances in high-resolution imagery and digital elevation models (DEMs) allow us to improve our capability in structural analysis, by expanding the number of observations to more reliably solve for the fault plane using a least squares minimisation.

3. Case Study I: The 2010 El Mayor-Cucapah Earthquake

The method described in section 2 is tested on the Pescadores fault (Figure 2) that ruptured in the 2010 M_w 7.2 El Mayor-Cucapah earthquake [Wei et al., 2011; Oskin et al., 2012]. We acquired Pleiades stereo imagery in 2014 and demonstrated that the accuracy of the surface topography derived from it is comparable to that of the lidar survey [Parsons et al., 2014; Zhou et al., 2015b]. We chose the Pescadores fault as a test study because the fault trace is relatively straight and simple, and the dip has been measured in the field in detail

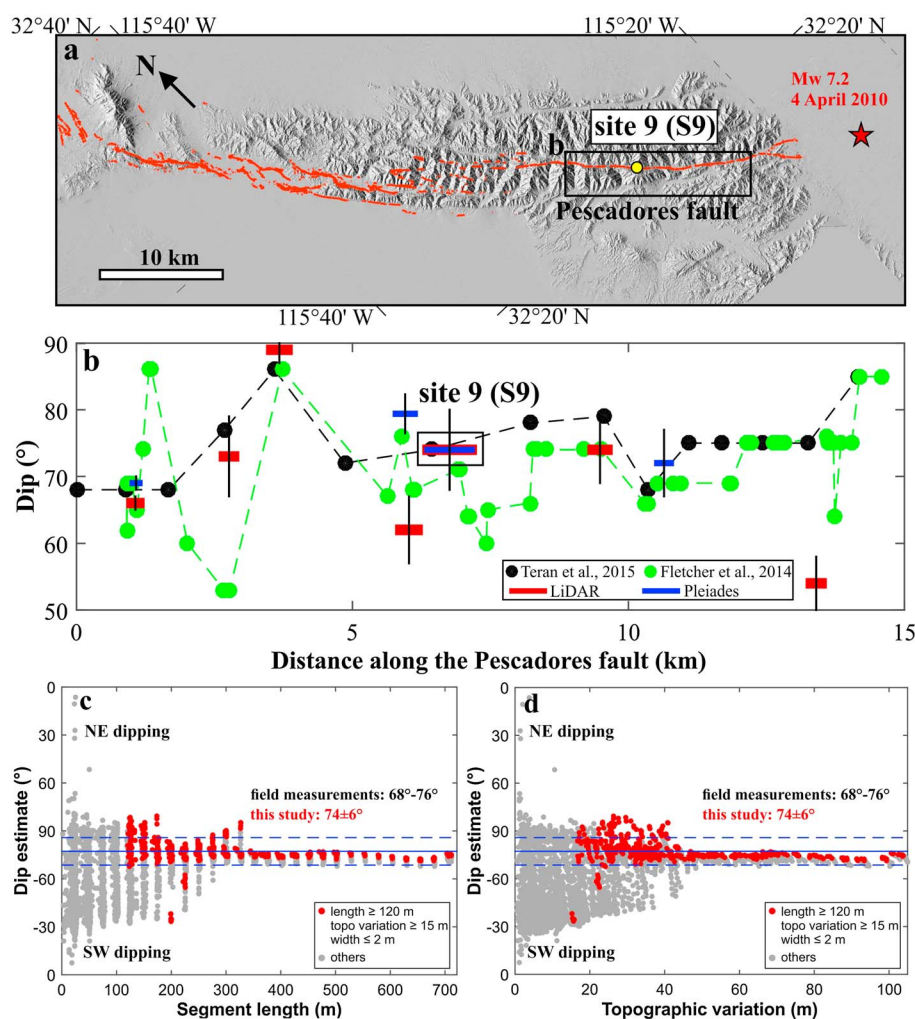


Figure 2. Estimate of dip of the Pescadores fault in Mexico from the downsampled lidar and Pleiades point clouds. (a) Shaded-relief pre-earthquake lidar digital elevation model (DEM) showing the epicentral area of the 2010 El Mayor-Cucapah earthquake (red star). Faults (red lines) are from Teran *et al.* [2015]. Site 9 (S9 in Table S1) was selected to test the influence of segment length, width, and topographic variation on the estimate of fault dip. (b) Dip estimates along the Pescadores fault from field measurements (green dots connected by the green dashed line are measured by Fletcher *et al.* [2014] and black dots connected by the black dashed line are measured by Teran *et al.* [2015]), Pleiades DEM (blue lines), and postearthquake lidar DEM (red lines) from this study. The length of the red and blue lines indicates the length of the segments used for fitting the fault plane. See Table S1 and Figure S1 for details. (c–d) Estimates of fault dip for site 9 from our Pleiades data by subsampling segment S9 are shown in Table S1. In Figure 2c the influence of segment length on the dip estimates. In Figure 2d the influence of topographic variation on the dip estimates. Red dots indicate the estimates from the 3-D points with a length of ≥ 120 m and topographic variation of ≥ 15 m extracted with polygons narrower than 2 m. Grey dots are the estimates from other segments. Field dip measurements of 68° – 76° are from Fletcher *et al.* [2014] and Teran *et al.* [2015]. Positive dip means northeast dipping, and negative means southwest dipping. Blue solid and dashed lines are the mean and standard deviation of the dip estimates in red.

[Fletcher *et al.*, 2014; Teran *et al.*, 2015]. By combining the coseismic displacement field [Barišin *et al.*, 2015], the imagery and the postearthquake lidar DEM, we are able to locate the surface rupture accurately.

The Pleiades imagery, which was acquired 4 years after the earthquake, does not show the surface rupture very clearly along parts of its length, so in order to avoid any ambiguities in fault identification, we only traced four unambiguous segments from the Pleiades imagery. Another seven segments were mapped from the shaded-relief lidar DEM (acquired 4 months after the earthquake) in which the rupture trace is very fresh and clear. Given the fact that point clouds derived from satellite stereo imagery (such as the 70 cm resolution Pleiades imagery) may have a lower density than high-resolution lidar surveys (>1 sample/m²), we downsampled the postearthquake lidar point cloud from ~ 10 samples/m² to 1 sample/m² to make it comparable.

Fault dip was estimated at these 11 segments by determining the best fitting fault plane to the 3-D coordinates of all the points within the segments (in WGS84-based Universal Transverse Mercator zone 11°N) along the surface fault trace (Table S1).

In the case of terrestrial lidar scans, fault planes can be reliably determined with points within a relatively small segment, due to its high accuracy—normally on the order of millimeter, and great point density, ≥ 1000 samples/m² [Gold *et al.*, 2013]. However, when using lower resolution and less accurate airborne lidar (submeter resolution and centimeter-level accuracy) and satellite-derived (1–2 m resolution and decimetric accuracy) topography, points from a longer fault segment are needed. Here we test the sensitivity of our method to the input data, i.e., the length and topographic variation of the fault segment to use. At site 9 (S9 in Table S1) where we remotely mapped a 800 m long surface rupture from the Pleiades imagery (Figure 2), we applied the following steps to subsample this section of the fault and estimate the dip. We started with a polygon 25 m long (L) and 0.5 m wide (W), centered on the rupture trace. We randomly chose 100 positions along the rupture and generated a new same-sized polygon for extracting 3-D points beginning at each new position, given that the trace of the fault along irregular topography is not the same. The dip and topographic variation (elevation difference between the highest and lowest points) were estimated for each set of points. We also determined the distance between the most extreme points in the point cloud that were included within the polygon each time. We then repeated the calculation varying L from 25 m to 800 m in steps of 25 m and varying W from 0.5 m to 5 m in steps of 0.5 m, placing our polygon in 100 random locations for each polygon size. In theory, this would give us 32,000 separate dip estimates. However, if our polygon was more than 25 m longer than the distance between the two most extreme points included within that polygon, then that estimate was discarded; these estimates are already likely to be included in previous calculations with smaller L. The result for S9 is plotted in Figures 2c and 2d. The estimates of dip vary significantly from 10° to 90° for segments shorter than 100 m (these short segments also have a low topographic variation of <10 m). As the length and topographic variation increase, the estimate becomes increasingly consistent and reliable, compared to the field measurements of 68° [Fletcher *et al.*, 2014] to 76° [Teran *et al.*, 2015]. The test also shows that fault segments of longer than 300 m (such segments also have a topographic variation of larger than 40 m at S9) can constrain the dip very well, but these segments are not usually available in other places. However, ~80% of the estimates from the segments with a topographic variation of ≥ 15 m and a length of ≥ 120 m agree with the field measurements (Figure 2c and 2d), and we therefore suggest these values as the minimum requirements for our method using these kinds of airborne and satellite DEM point clouds. In addition, to extract points from a point cloud using a polygon, a width of ≤ 2 m is also preferred as wider polygons may include a large number of outliers that do not lie on the fault plane. Longer segments with larger topographic variation may better constrain the least squares regression and hence the dip estimate, but as fault dip may vary significantly over a length scale of a kilometer, we also suggest a maximum length of 1 km to avoid oversmoothing of the estimate of the dip. Similarly, we subsampled all the other segments (see Figure S1) and the proposed criteria yielded very consistent results. As shown in Figure 2b, the difference between our estimates and those in Teran *et al.* [2015] (at the same locations) is $-9 \pm 12^\circ$; the difference between our estimates and those in Fletcher *et al.* [2014] is $2 \pm 8^\circ$. The estimate of dip is not sensitive to the formal error on the orthogonal distance d_i , so the dip error from the least squares regression is tiny ($\leq 1^\circ$). In the end, we used the standard deviation of all the estimates from the subsampling segments as the error bounds (i.e., bootstrapping in regression problems [Efron, 1979]).

It should be noted that our dip estimates represent the fault geometry over a length scale of hundreds of meters, while field measurements from outcrops describe the fault at meter scale, and modeling from coseismic surface displacements determines the fault geometry over tens of kilometers. This method therefore provides a useful intermediate scale.

4. Case Study II: The 2013 Balochistan Earthquake

The 2013 M_w 7.7 Balochistan, Pakistan earthquake ruptured a 200+ km section of the arcuate and moderately dipping (50°–70° N) Hoshab fault in the eastern Makran accretionary wedge [Avouac *et al.*, 2014; Jolivet *et al.*, 2014; Zhou *et al.*, 2015a] (Figure 3). The rupture was bilateral but propagated much further to the south of the epicenter than to the north (Figure 3c) where fault creep (~ 3 mm/yr) has released a large fraction of the accumulated stress [Fattahi *et al.*, 2014]. Subpixel matching of pre-earthquake and postearthquake Landsat-8 imagery reveals an average of ~ 8 m left-lateral strike-slip motion during the earthquake [Avouac *et al.*, 2014] (as reproduced in Figure 3c).

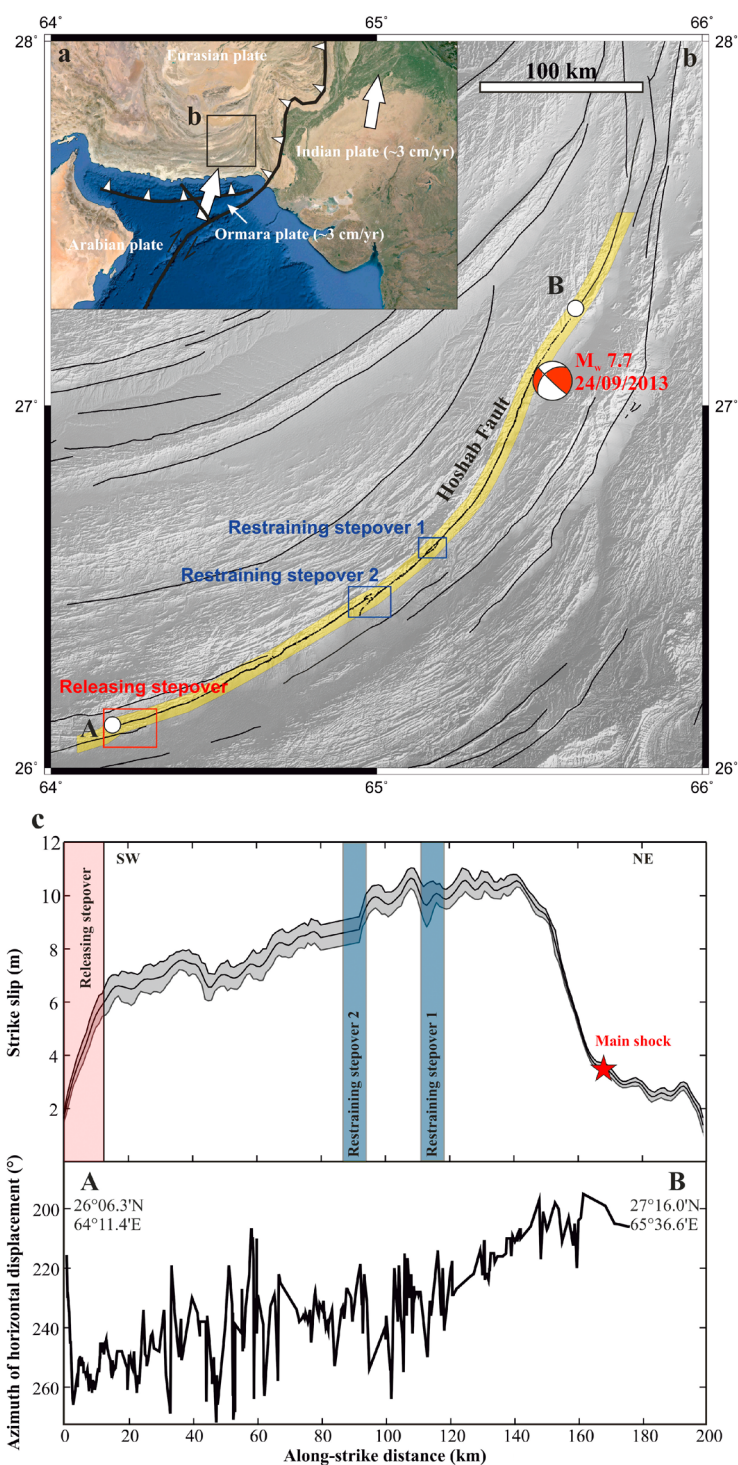


Figure 3. Tectonic setting of the 2013 Balochistan, Pakistan earthquake in the eastern Makran accretionary wedge. (a) The eastern Makran is a kinematic transition zone [Zhou *et al.*, 2015a] between subduction of the Ormara plate beneath Eurasia at ~3 cm/yr in the west [Kukowski *et al.*, 2000; Bilham *et al.*, 2007] and northward motion of the Indian plate with respect to Eurasia at ~3 cm/yr in the east [Szeliga *et al.*, 2012]. (b) Yellow polygon denotes the coverage of the postearthquake Pleiades imagery. (c) Surface strike-slip displacement in the 2013 earthquake derived from cross-correlating pre-earthquake and postearthquake Landsat-8 imagery [Avouac *et al.*, 2014]. Blue boxes show two restraining stepovers, which have been identified in previous studies. These restraining stepovers did not appear to influence the rupture process. We have identified a stepover at the end of the main trace (red box). The surface slip decreased abruptly to zero from 6 m over ~15 km across this stepover. The azimuth of horizontal displacement was measured from visual analysis of offset geomorphic features.

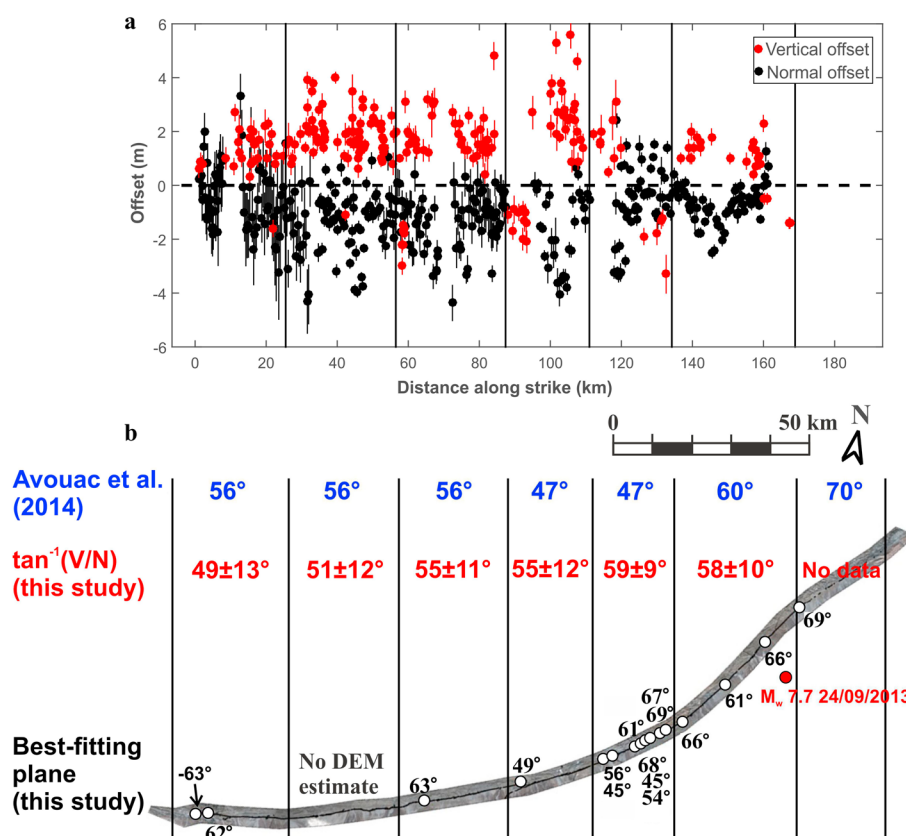


Figure 4. (a) Vertical and fault-normal offsets in the 2013 Balochistan earthquake. Vertical offsets are from Zhou et al. [2015a]. Fault-normal offsets are calculated from the displacement field obtained by cross-correlating pre-earthquake and postearthquake WorldView images [Barnhart et al., 2015]. (b) Dip estimates along the Hoshab fault from our study (numbers in black, positive for north dipping; see S12–S27 in Table S1 and Figure S1 for details), the inversion result of global low-frequency W-phase waveforms (numbers in blue at the top) [Avouac et al., 2014], and the method by combining the average vertical (V) and fault-normal (N) offsets along each segment (numbers in red near the top). White dots denote the sites where we calculated the fault dip from the Pleiades topography. Black vertical lines indicate fault segmentation prescribed in the modeling [Avouac et al., 2014].

Two restraining stepovers (1.5 km wide and 0.7 km wide at 26.5° N, 65.0° E and 26.6° N, 65.2° E, respectively) have been previously identified along the 200+ km surface rupture in the 2013 earthquake [Avouac et al., 2014] (Figure 3b). The stepovers are small enough that they are unlikely to represent discontinuities at depth, and the rupture propagated through them without interruption (Figure 3c). No clear geometrical control on the rupture process has been observed to date [Avouac et al., 2014]. We use the method described in the previous sections to examine the 3-D fault geometry.

We first mapped the rupture trace based on the postearthquake Pleiades imagery and the topography derived from it [Zhou et al., 2015a]. To avoid unreliable estimates, fault dip was only calculated along simple surface ruptures with only a single strand. For each segment (>120 m in length and with a topographic variation of ≥ 15 m), we used a set of points along the rupture and ran the random subsampling described in section 3 to estimate the best fitting fault plane. Fault dips along the rupture are summarized in Table S1 and Figure S1. The dip varies from 69°N in the northern section, where the rupture was initiated, to 62° N in the southern section, in good agreement with the joint inversion result of coseismic geodetic observations and global low-frequency W-phase waveforms [Avouac et al., 2014; Jolivet et al., 2014] (Figure 4). For comparison, we also estimated the average dip (θ) of each fault segment (fault segments are defined by Avouac et al. [2014]) by combining vertical (V) and fault-normal (N) offsets using the relationship $\theta = \tan^{-1} \frac{V}{N}$ [Zhou et al., 2015b]. To obtain the fault-normal offsets, we resolved the east-west and north-south components of the surface displacement from Barnhart et al. [2015] onto the fault-normal direction. Weighting by the uncertainties of the offsets (Figure 4a), we obtained average vertical/fault-normal offsets of 1.4 ± 0.6 m/ 1.2 ± 0.3 m, 2.0 ± 0.7 m/ 1.6 ± 0.3 m, 2.0 ± 0.8 m/ 1.4 ± 0.2 m, 2.7 ± 1.2 m/ 1.9 ± 0.2 m, 2.0 ± 0.8 m/ 1.2 ± 0.1 m,

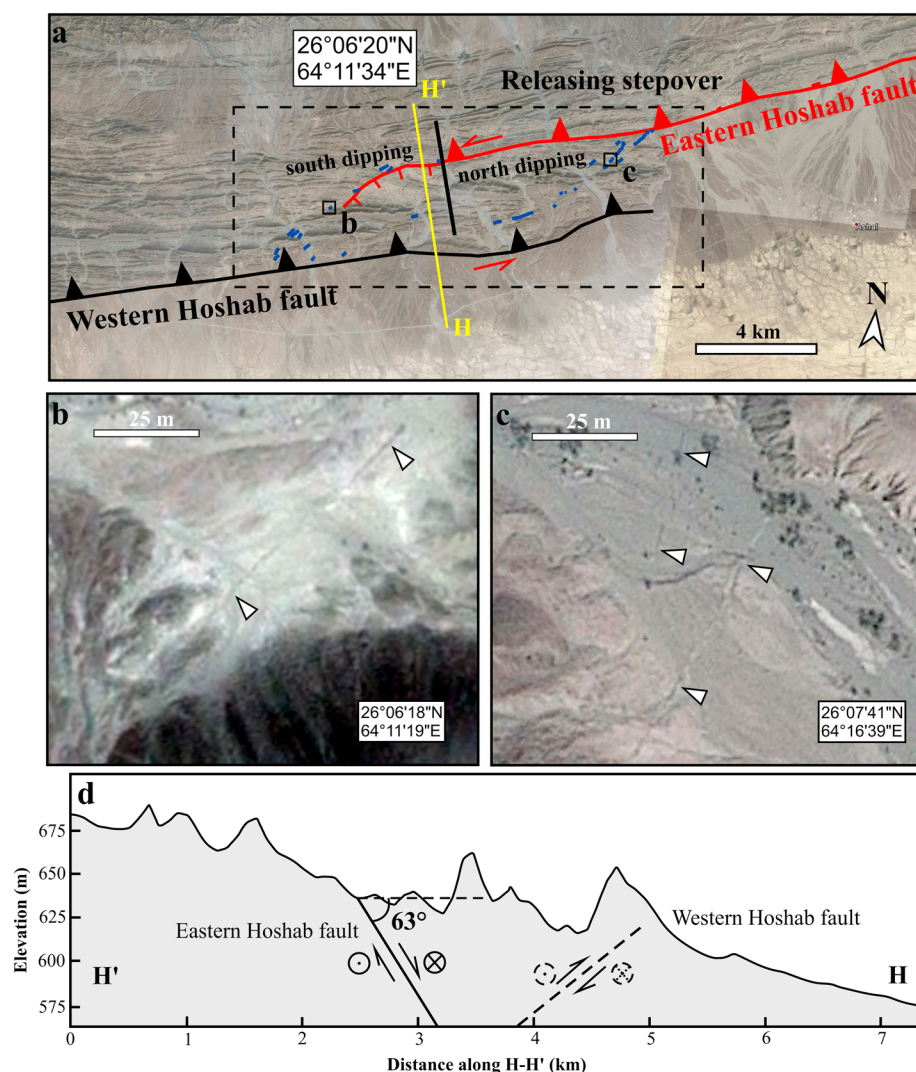


Figure 5. Termination of the 2013 rupture at the southern end of the Hoshab fault. (a) Google Earth imagery (17 December 2013) showing the stepover (see Figure 3b for location). Red line denotes the surface rupture in the 2013 earthquake. Black line denotes the Western Hoshab fault. We did not find any clear evidence for surface ruptures on this western fault. Blue lines indicate surface cracks within the stepover. (b and c) Postearthquake Pleiades imagery showing surface fractures (indicated by the white arrows) in the stepover. (d) Elevation profile (from the 90 m Shuttle Radar Topography Mission DEM) along H-H' shows long-term deformation on the western Hoshab fault.

and 1.3 ± 0.5 m/ 0.8 ± 0.1 m for each fault segment (from south to north); the corresponding dips are estimated to be $49 \pm 13^\circ$, $51 \pm 12^\circ$, $55 \pm 11^\circ$, $55 \pm 12^\circ$, $59 \pm 9^\circ$, and $58 \pm 10^\circ$ (Figure 4b). The three independent estimates are consistent within the estimated error (Figure 4b), except for the fifth segment (from south to north) where we found a slightly larger difference (12°) between our estimates and those of *Avouac et al.* [2014]. The estimates obtained by determining a best fitting plane show a variation from 45° to 69° along this segment, in which case average estimates of fault dip over tens of kilometers may have oversmoothed the fault structure at the surface (from $\theta = \tan^{-1} \frac{V}{N}$), as well as at depth (from *Avouac et al.* [2014]). The observed inconsistency is likely to have resulted from oversmoothing and therefore suggests that estimates of fault dip at different scales are necessary to investigate 3-D fault structure in the near surface.

The surface trace of the 2013 earthquake appears to be relatively continuous (despite the two small restraining stepovers) (Figure 3), and the fault geometry (dip) appears to be smooth with gradual changes on a spatial scale of tens of kilometers (Figure 4b), which leads to an open question as to why the rupture suddenly stopped in the south with the surface displacement decreasing from 6 m to zero within a 12 km zone. By estimating the dip at a smaller scale with our method, we found a 3.7 km long segment dipping 63° S (Figure S1)

with north side up left-lateral normal slip at the end of the main trace, which we interpret to be a response to localized extension (Figure 5a). On closer examination, we identified many discontinuous surface cracks within the stepover (Figures 5b and 5c), but the rupture did not propagate onto the previously unmapped western fault. The 2013 rupture ended in a stepover (3 km wide, 12 km long). This stepover could have resulted from the oblique orientation that the main Hoshab fault has to the regional slip vector [Cunningham and Mann, 2007]. It is also possible that this is a relay stepover due to strike-slip motion on the overlapping western and eastern strands [Peacock and Sanderson, 1991]. The abrupt decrease in surface slip from 6 m across the stepover (Figure 3c) indicates that this stepover has significantly dissipated seismic energy. The high topographic relief across the western fault shows long-term deformation (Figure 5d), but there is no clear evidence for surface ruptures from past earthquakes. We therefore suggest that this previously unidentified stepover (with a significant change in fault dip) may act as the endpoint of earthquake ruptures on the Hoshab fault [King and Nábelek, 1985; Wesnousky, 2006].

5. Conclusions

We have demonstrated the utility of airborne lidar and satellite optically derived high-resolution topography to calculate fault dip by fitting planes to the 3-D surface trace. Examples from the 2010 El Mayor-Cucapah (Mexico) and 2013 Balochistan (Pakistan) earthquakes show that this classic structural geology approach works very well on the newly derived high-resolution topography when compared to estimates from previous geodetic inversions [Wei et al., 2011; Avouac et al., 2014; Jolivet et al., 2014] and field measurements [Fletcher et al., 2014; Teran et al., 2015] and can recover variations in dip at a spatial resolution of hundreds of meters to kilometers. To ensure a reliable dip estimate, we suggest a minimum segment length of 120 m with a minimum topographic variation of 15 m for 1 m resolution topographic data derived from satellite stereo imagery such as Pleiades. For lidar scans with higher point densities, it would be possible to use shorter fault segments. We also avoided complicated rupture zones where the fault is not a single trace on the surface, which is a common case when a fault cuts through unconsolidated soft materials, e.g., the Paso Superior detachment in the El Mayor-Cucapah case [Teran et al., 2015], as they may give misleading results.

The case study of the 2013 Balochistan, Pakistan earthquake suggests that small-scale features such as variations in along-strike fault dip may be essential to identify and investigate geometrical controls on earthquake ruptures. No significant geometrical complexity has been observed in previous studies of the 2013 earthquake [Avouac et al., 2014; Jolivet et al., 2014; Barnhart et al., 2014]. However, by calculating the 3-D fault geometry, we found a variation in dip at the end of the main trace within a stepover. This stepover may act as the end point of earthquake ruptures in the south of the Hoshab fault. Applied to future earthquakes, or any faults with traces and other planar markers (such as bedding planes) at the surface, lidar surveys and Pleiades as well as other (submeter) VHR (such as WorldView and GeoEye) stereo imagery will provide detailed information about fault geometry to complement field-based observations and modeling results, which can be very useful in dynamic modeling of earthquake rupture [Harris, 2004], hazard assessment of older fault zones, mapping, and mining exploration.

References

- Avouac, J.-P., et al. (2014), The 2013, M_w 7.7 Balochistan earthquake, energetic strike-slip reactivation of a thrust fault, *Earth Planet. Sci. Lett.*, **391**, 128–134.
- Barišić, I., A. Hinojosa-Corona, and B. Parsons (2015), Co-seismic vertical displacements from a single post-seismic lidar DEM: Example from the 2010 El Mayor-Cucapah earthquake, *Geophys. J. Int.*, **202**(1), 328–346.
- Barnhart, W., G. Hayes, R. Briggs, R. Gold, and R. Bilham (2014), Ball-and-socket tectonic rotation during the 2013 M_w 7.7 Balochistan earthquake, *Earth Planet. Sci. Lett.*, **403**, 210–216.
- Barnhart, W., R. Briggs, N. Reitman, R. Gold, and G. Hayes (2015), Evidence for slip partitioning and bimodal slip behavior on a single fault: Surface slip characteristics of the 2013 M_w 7.7 Balochistan, Pakistan earthquake, *Earth Planet. Sci. Lett.*, **420**, 1–11.
- Bilham, R., S. Lodi, S. Hough, S. Bukhary, A. M. Khan, and S. Rafeeqi (2007), Seismic hazard in Karachi, Pakistan: Uncertain past, uncertain future, *Seismol. Res. Lett.*, **78**(6), 601–613.
- Cunningham, W., and P. Mann (2007), Tectonics of strike-slip restraining and releasing bends, *Geol. Soc. London., Spec. Pub.*, **290**(1), 1–12.
- Efron, B. (1979), Bootstrap methods: Another look at the jackknife, *Ann. Probab.*, **7**(1), 1–26.
- Elliott, A. J., M. E. Oskin, J. Liu-Zeng, and Y. Shao (2015), Rupture termination at restraining bends: The last great earthquake on the Altyn Tagh Fault, *Geophys. Res. Lett.*, **42**(7), 2164–2170.
- Elliott, J. R., E. K. Nissen, P. C. England, J. A. Jackson, S. Lamb, Z. Li, M. Oehlers, and B. Parsons (2012), Slip in the 2010–2011 Canterbury earthquakes, New Zealand, *J. Geophys. Res.*, **117**, B03401, doi:10.1029/2011JB008868.
- Fattahi, H., F. Amelung, E. Chaussard, S. Wdowinski, and T. Dixon (2014), Characterizing seismic and aseismic deformation along the Chaman fault system with InSAR, Abstract G11A-0463 presented at 2014 Fall Meeting, vol. 1, pp. 0463, AGU, San Francisco, Calif.

Acknowledgments

The postearthquake lidar data was collected by the National Center for Airborne Laser Mapping at the request of Michael Oskin (UC Davis) in collaboration with Alejandro Hinojosa and John Fletcher of CICESE and Ramon Arrowsmith of Arizona State University and downloaded from OpenTopography (<http://dx.doi.org/10.5069/G9TD9V7D>). The scripts for estimating fault dip based on random subsampling are freely available from Yu Zhou. This work was supported by the University of Oxford through a PAG scholarship to Yu Zhou and the Natural Environment Research Council through the Looking into the Continents from Space project (NE/K011006/1) and the Centre for the Observation and Modelling of Earthquakes, Volcanoes and Tectonics (COMET). We thank Austin Elliott, Tim Middleton, and David Mackenzie for discussions on fault geometry and stepovers and William Barnhart for providing the coseismic surface displacement of the 2013 Balochistan earthquake. We also thank John Fletcher and two anonymous reviewers for their insightful reviews.

- Fletcher, J. M., et al. (2014), Assembly of a large earthquake from a complex fault system: Surface rupture kinematics of the 4 April 2010 El Mayor–Cucapah (Mexico) M_w 7.2 earthquake, *Geosphere*, 10(4), 797–827.
- Gold, P. O., M. E. Oskin, A. J. Elliott, A. Hinojosa-Corona, M. H. Taylor, O. Kreylos, and E. Cowgill (2013), Coseismic slip variation assessed from terrestrial LiDAR scans of the El Mayor–Cucapah surface rupture, *Earth Planet. Sci. Lett.*, 366, 151–162.
- Harris, R. A. (2004), Numerical simulations of large earthquakes: Dynamic rupture propagation on heterogeneous faults, *Pure Appl. Geophys.*, 161(11–12), 2171–2181.
- Harris, R. A., and S. M. Day (1999), Dynamic 3D simulations of earthquakes on en echelon faults, *Geophys. Res. Lett.*, 26(14), 2089–2092.
- Jolivet, R., et al. (2014), The 2013 M_w 7.7 Balochistan earthquake: Seismic potential of an accretionary wedge, *Bull. Seismol. Soc. Am.*, 104(2), 1020–1030.
- Kase, Y., and S. M. Day (2006), Spontaneous rupture processes on a bending fault, *Geophys. Res. Lett.*, 33, L10302, doi:10.1029/2006GL025870.
- King, G., and J. Nábelek (1985), Role of fault bends in the initiation and termination of earthquake rupture, *Science*, 228(4702), 984–987.
- Kukowski, N., T. Schillhorn, E. R. Flueh, and K. Huhn (2000), Newly identified strike-slip plate boundary in the northeastern Arabian Sea, *Geology*, 28(4), 355–358.
- Lozos, J. C., D. D. Oglesby, J. N. Brune, and K. B. Olsen (2012), Small intermediate fault segments can either aid or hinder rupture propagation at stepovers, *Geophys. Res. Lett.*, 39, L18305, doi:10.1029/2012GL053005.
- Oskin, M. E., et al. (2012), Near-field deformation from the El Mayor–Cucapah earthquake revealed by differential LIDAR, *Science*, 335(6069), 702–705.
- Parsons, B., Y. Zhou, J. R. Elliott, I. Barisin, and R. T. Walker (2014), Assessing the ability of Pleiades stereo imagery to determine height changes in earthquakes: A case study for the El Mayor–Cucapah epicentral area, Abstract EP43E-08, presented at 2014 Fall Meeting, pp. 8, AGU.
- Peacock, D., and D. Sanderson (1991), Displacements, segment linkage and relay ramps in normal fault zones, *J. Struct. Geol.*, 13(6), 721–733.
- Sudhaus, H., and S. Jónsson (2011), Source model for the 1997 Zirkuh earthquake ($M_w=7.2$) in Iran derived from JERS and ERS InSAR observations, *Geophys. J. Int.*, 185(2), 676–692.
- Szeliga, W., R. Bilham, D. M. Kakar, and S. H. Lodi (2012), Interseismic strain accumulation along the western boundary of the Indian subcontinent, *J. Geophys. Res.*, 117, B08404, doi:10.1029/2011JB008822.
- Tearpock, D. J., and R. E. Bischke (2002), *Applied subsurface geological mapping with structural methods*, Pearson Education, Prentice Hall, Upper Saddle River, N. J.
- Teran, O. J., et al. (2015), Geologic and structural controls on rupture zone fabric: A field-based study of the 2010 M_w 7.2 El Mayor–Cucapah earthquake surface rupture, *Geosphere*, 11(3), 899–920.
- Wei, S., et al. (2011), Superficial simplicity of the 2010 El Mayor–Cucapah earthquake of Baja California in Mexico, *Nat Geosci.*, 4(9), 615–618.
- Wesnousky, S. G. (2006), Predicting the endpoints of earthquake ruptures, *Nature*, 444(7117), 358–360.
- Zhou, Y., J. R. Elliott, B. Parsons, and R. T. Walker (2015a), The 2013 Balochistan earthquake: An extraordinary or completely ordinary event?, *Geophys. Res. Lett.*, 42, 6236–6243, doi:10.1002/2015GL065096.
- Zhou, Y., B. Parsons, J. R. Elliott, I. Barisin, and R. T. Walker (2015b), Assessing the ability of Pleiades stereo imagery to determine height changes in earthquakes: A case study for the El Mayor–Cucapah epicentral area, *J. Geophys. Res. Solid Earth*, 120, 8793–8808, doi:10.1002/2015JB012358.